Nano Energy 35 (2017) 396–404

Contents lists available at ScienceDirect

Nano Energy

journal homepage: www.elsevier.com/locate/nanoen

Full paper

Novel layer-by-layer stacked VS_2 nanosheets with intercalation pseudocapacitance for high-rate sodium ion charge storage

Ruimin Sun[a], Qiulong Wei[a], Jinzhi Sheng[a], Changwei Shi[a], Qinyou An[a,*], Sijie Liu[a], Liqiang Mai[a,b,**]

[a] State Key Laboratory of Advanced Technology for Materials Synthesis and Processing, Wuhan University of Technology, Luoshi Road 122, Wuhan 430070, PR China

[b] Department of Chemistry, University of California, Berkeley, CA 94720, United States

ARTICLE INFO

Keywords:
VS_2
Sodium ion batteries
Transition metal dichalcogenides (TMDs)
Anode
Intercalation pseudocapacitance

ABSTRACT

Sodium ion batteries (SIBs) have been considered as a promising candidate for large scale energy storage systems due to their low cost and reasonable performance. However, developing desirable anode materials with high capacity, excellent cycling stability and high rate capability remains great challenges. Herein, novel layer-by-layer VS_2 stacked nanosheets (VS_2-SNSs) are synthesized using a facile one-step polyvinylpyrrolidone (PVP) assisted assembly method. With a highly stable orderly stacked layer structure, the VS_2 delivers excellent electrochemical performance in SIBs. A reversible discharge capacity of 250 mA h g^{-1} is obtained at 0.2 A g^{-1}. A high specific capacity of 150 mA h g^{-1} even at 20 A g^{-1} is reached (discharged/charged in 27 s). Furthermore, the VS_2-SNSs deliver long cycling life with almost no capacity fading even after 600 cycles at 5 A g^{-1}. *In-situ* XRD and *ex-situ* TEM characterization reveal that VS_2 undertakes a reversible intercalation reaction mechanism. A detailed electrochemical kinetic analysis reveals that the sodium ion charge storage depends on intercalation pseudocapacitive behavior with a high capacitive contribution up to 69% for the total capacity at 1 mV s^{-1}. The impressive electrochemical performance reveals that the VS_2 has great potential for the next generation large scale energy storage.

1. Introduction

Green energy storage has attracted numerous attention and is rapidly developed for various technological applications, such as portable electronic devices and electric vehicles [1–4]. Recently, sodium ion batteries (SIBs) are considered as an alternative to lithium ion batteries (LIBs) due to low cost and earth abundance of sodium [5–7]. Many cathode materials for sodium ion storage, such as layered transition metal oxides [8,9], polyanionic compounds [10–12], and so forth, have been developed with superior electrochemical performance. However, in the case of anode materials, the commercial graphite exhibits a very low capacity of 35 mA h g^{-1} in SIBs [13]. The alloy-type (Sn [14], P [15], SnO_2 [16], *etc.*) and conversion type (ZnO [17], CoS [18], *etc.*) anodes exhibit high capacity but poor cycling and rate performance. Therefore, it is urgent to find desirable anode materials with great cycling stability, long life and high rate performance. The outstanding properties of graphene have aroused the interest in other two-dimensional (2D) layered materials, including transition metal oxides (TMOs) and transition metal dichalcogenides (TMDs) [19]. The later recently have received much attention owing to their unique physical and chemical properties [20,21], which are developed for the applications of energy storage [22–24], catalysis [25], light harvesting [26], electronics [27], *etc.*

VS_2 is one of the TMDs, was first discovered in 1970s [28]. The VS_2 crystal is made up of a metal vanadium sandwiched between the two sulfide layers as S-V-S. These triple layers stack together by weak Van der Waals force to form a layered structure with an interlayer spacing of 5.76 Å [29]. This structure provides a loosely stacked framework that the interlayer distance of VS_2 is much larger than the ionic diameter of Na^+ (1.96 Å). The large open channels between the layers offer potential sites for alkali metals insertion and extraction and the metallic property is beneficial for charge transfer [30]. In addition, being cheap and source abundant, VS_2 has great superiority for practical energy storage applications [31].

Pseudocapacitive charge storage is another important type of energy storage mechanism that reversible faradaic reactions lead to

* Corresponding author.
** Corresponding author at: State Key Laboratory of Advanced Technology for Materials Synthesis and Processing, Wuhan University of Technology, Luoshi Road 122, Wuhan 430070, PR China.
E-mail addresses: anqinyou86@whut.edu.cn (Q. An), mlq518@whut.edu.cn (L. Mai).

http://dx.doi.org/10.1016/j.nanoen.2017.03.036
Received 27 August 2016; Received in revised form 10 March 2017; Accepted 16 March 2017
Available online 08 April 2017

high power density but also energy density [32]. These charge transfer reactions occur at the surface or near-surface of the active material, associated with fast redox reactions, which are able to offer high specific capacitance more than 1000 F g^{-1} [33,34]. Thus, designing novel pseudocapacitive electrodes is highly expected for energy storage. TMDs are promising pseudocapacitive candidates due to their large interlayer spaces that allow for fast ion diffusion [20,35]. However, they have not been well researched at this behavior because most reports focus on their high capacity. For example, the mostly studied MoS_2 with a conversion reaction delivered a high specific capacity of 854 mA h g^{-1} at 0.1 A g^{-1}, but accompanying with severely volume expansion and sluggish kinetics for the reformation of the active materials and the damage of diffusion pathway [36,37]. In fact, the intercalation or conversion reaction would occur in charge storage process, which is controlled by the terminal discharge voltage and the insertion number of Na^+ [38]. Therefore, by limiting the discharge-charge voltage window, the batteries could follow intercalation type reaction that the cyclability will be improved. In the 1980s, Abraham and co-workers reported that VS_2 exhibited intercalation properties in the Na system utilized β-Al_2O_3 solid electrolyte at high temperature, but there is no convictive evidence to further prove it clearly and the long-term cyclability, high-rate capability of this electrode material at room temperature still need to be further explored [39]. For intercalation-type anodes, the balance between structure stability and capacity needs to be taken into account. Recently, Dunn and co-workers presented that two dimensional layered TiS_2 and mesoporous MoS_2 both exhibited Li^+ or Na^+ intercalation pseudocapacitive charge storage behavior [20,35]. They pointed that decreasing the particle size is one route to realize pseudocapacitive behavior, since the ions diffusion path lengths are largely shortened by reducing the size of material. However, up to now, the layered VS_2 applied as room temperature SIBs and its detailed charge storage mechanism remain unexplored.

Herein, we present a novel layer-by-layer VS_2 stacked nanosheets (VS_2-SNSs) which synthesized using a facile one-step polyvinylpyrrolidone (PVP) assisted assembly method. Such novel layer-by-layer stacked nanosheets would provide stable framework for the volume swelling/shrink during ions insertion/extraction, leading to the long term cycling stability. The considerable amounts of pores between the layers result in fast Na^+ diffusion and thus high-rate capability. When evaluated as SIBs anode, the VS_2-SNSs exhibit a reversible discharge capacity of 250 mA h g^{-1} at 0.2 A g^{-1}. A specific capacity of 150 mA h g^{-1} is reached even at an ultrahigh current density of 20 A g^{-1} (discharged/charged in 27 s), suggesting the remarkable high-rate capability. The electrode delivers long lifetime with excellent capacity retention even after 600 cycles at 5 A g^{-1}. The use of *in-situ* X-ray diffraction (XRD) and *ex-situ* transmission electron microscopy (TEM) enables us to connect the excellent electrochemical behavior in VS_2-SNSs to the structure changes occurring during the electrochemical process. Furthermore, a detailed electrochemical kinetic analysis is performed to explore the nature of the charge storage process.

2. Experimental section

All the reagents used in the experiment were of analytical grade and used without further purification.

2.1. Sample preparation

Synthesis of VS_2-SNSs and VS_2-MNSs: In a typical synthesis, 1g PVP K-30 was first dissolved in the mixture of 30 ml distilled water and 2 ml ammonium hydroxide. Then 2 mmol NH_4VO_3 was dissolved in sequence with continuous stirring. Then 20 mmol C_2H_5NS (TAA) was added. The solution kept stirring 1 h at room temperature. After that, the solution was loaded into a Teflon-lined sealed autoclave and maintained at 180 °C for 20 h. The obtained suspension was centrifuged and the product was washed thoroughly with distilled water and ethanol several times and then dried at 60 °C in a vacuum oven for 12 h. Finally, the products were annealed at 300 °C for 2 h to obtain VS_2-SNSs. For comparison, the VS_2-MNSs were synthesized using the same procedure without the addition of PVP K-30.

2.2. Materials characterization

In-situ X-ray diffraction experiments during electrochemical measurement of the batteries were performed on a D8 Discover X-ray diffractometer with a nonmonochromated Cu K_α X-ray source scanned between 16° and 41° two theta ranges. An *in-situ* battery was designed with a Be window for X-ray penetration. XRD patterns of the samples were collected by using a D8 Advance X-ray diffractometer with Cu K_α X-ray source at room temperature. SEM images were collected with a JEOL-7100F microscope. TEM and HRTEM images were recorded using a JEM-2100F STEM/EDS microscope. Raman spectra were obtained using a Renishaw INVIA micro-Raman spectroscopy system. Brunauer Emmet-Teller surface area was measured by using Tristar II 3020 instrument.

2.3. Measurements of electrochemical performances

The electrochemical properties were performed with 2016 coin-type cells in an argon-filled glove box. Sodium disks were employed as the counter and reference electrodes. The working electrodes were fabricated on Cu foil current collectors. The slurry was obtained by mixing the as-synthesized materials, acetylene black and carboxyl methyl cellulose (CMC) binder in a weight ratio of 7:2:1. The mass loading of the electrode was 1.2–1.5 mg cm^{-2}. Glass fiber was employed as the separator. The electrolyte was composed of 1 M $NaSO_3CF_3$ dissolved in diglyme (DGM). Galvanostatic measurements were performed over a potential range of 0.4–2.2 V *vs.* Na^+/Na by using a multichannel battery testing system (LAND CT2001A). The Galvanostatic intermittent titration technique (GITT) experiment was performed between 0.4 and 2.2 V by appling a current of 20 mA g^{-1}. Cyclic voltammetry (CV) was tested by an electrochemical workstation (CHI 760D). Electrochemical impedance spectroscopy (EIS) was conducted with Autolab Potentiostat Galvanostat (PGSTAT302N). All of the measurements were carried out at room temperature.

2.4. Construction of a sodium-ion full cell

A sodium-ion full cell was constructed using VS_2 as the anode and $Na_3V_2(PO_4)_3$/C as the cathode in a 2016 coin-type cell. $Na_3V_2(PO_4)_3$/C cathode was prepared according to previous report [55]. The full cell was limited by the anode, in which the weight ratio of the two electrodes (anode/cathode) was 1:1.9–2. The electrolyte was 1 M $NaSO_3CF_3$ in diglyme (DGM). The full cells were charged and discharged between the voltage range of 1.2–3.0 V at various rates.

3. Results and discussions

Fig. 1a schematically illustrates the formation of layer-by-layer VS_2-SNSs. Time-depended reaction experiments were conducted. The scanning electron microscopy (SEM) images (Fig. S1) obtained at different reaction time demonstrate the evolution process. In the first 2 h, the numerous precursor nuclei form quickly. Then with the reaction increases to 6 h, the product becomes rough nanoparticles with fracture surface. After prolonged reaction for 10 h, the whole nanoparticles become uniform and the nanosheet subunits become clearer and tend to assemble together by an oriented attachment. At last, layer-by-layer VS_2-SNSs are completely formed. As is revealed by XRD patterns (Fig. S2) at different reaction time, our product obtained at the initial stage (2–6 h) is not the VS_2 phase. Along with the prolonged reaction time (10 h), the diffraction peaks of the impure phases become gradually weaker, whereas the peaks of the VS_2 phase

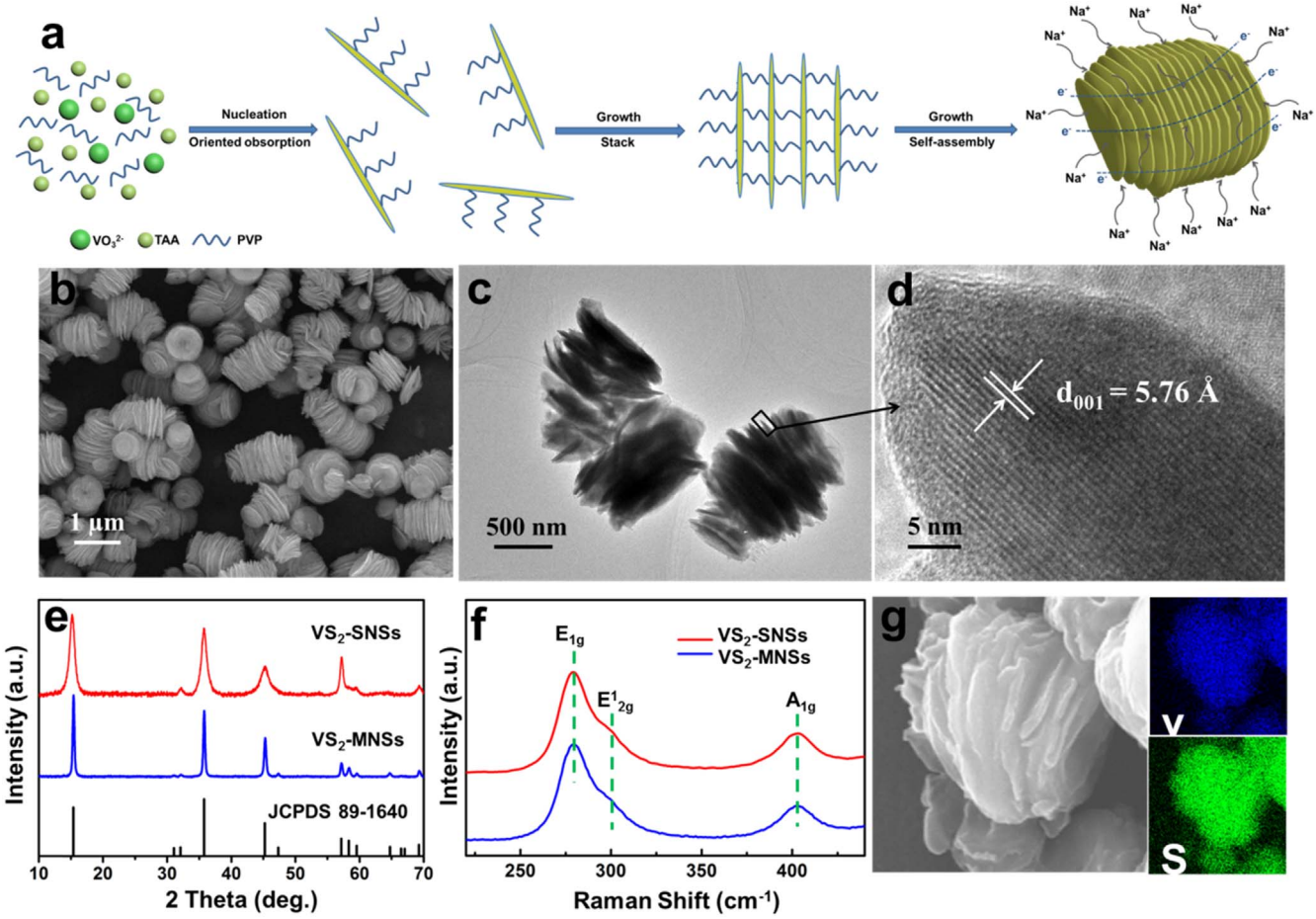

Fig. 1. (a) Schematic illustration of the formation of layer-by-layer VS_2-SNSs. (b) SEM image, (c) TEM image and (d) HRTEM image of VS_2-SNSs. (e) XRD patterns and (f) Raman spectra of VS_2-SNSs and VS_2-MNSs. (g) EDS elemental mapping of V and S, showing uniform elemental distribution.

become gradually stronger. Pure VS_2 forms when the reaction time is about 20 h. On the basis of above mentioned results, a possible formation mechanism is summarized as follows. The growth of VS_2 nanosheets is due to the anisotropic growth, since the large different surface energies of VS_2 facets. The crystal growth rate is different in each crystal direction with the principle of minimum energy. The (001) surface exhibits the lowest surface energy among the various facets of VS_2 structure [20]. The bonding between layers is weak, which is controlled by weak van der Waals force, not covalent bonding. With the increase of reaction time, coalescence of VS_2 sheets occurs and results in the subsequent growth along the *ab*-plane to form the VS_2 nanosheets [40]. Meanwhile, NH_4^+ from the NH_4VO_3 and ammonia in solution may absorb on the (001) facets of the VS_2 nanosheets, leading to the positively charged VS_2 nanosheets [31]. PVP has the hydroxyl groups at the ends of this molecules as an anionic surfactant and will absorb on the surface of VS_2 layers due to electrostatic interactions [41]. These adsorbed surfactant will be a linking agent to bridge adjacent VS_2 nanosheets together. Each nanosheet self-assembly with each other along the [001] direction and eventually forms the hierarchical layer-by-layer VS_2-SNSs structure [8,42–45]. The morphology of the layer-by-layer stacked VS_2 nanosheets with different PVP amounts during synthesis is shown in Fig. S3. With 0.5 g PVP addition, the stacked nanosheets are formed and assembled with each other, but the whole particle size is more than 1.5 μm. When the amount of PVP reaches 1 g, the morphology is uniform layer-by-layer stacked nanosheets. By continuing to increase the amount of PVP to 2 g, the stacked nanosheets are inhomogeneous and the surface becomes much rougher. To sum up, optimal layer-by-layer stacked nanosheets are obtained at the condition of 1 g PVP.

The SEM images (Figs. 1b and S4) are utilized to observe the shapes of VS_2-SNSs and VS_2 micron-sized nanosheets (VS_2-MNSs), respectively. The VS_2-SNSs are homogeneous with high quality and are composed of layer-by-layer stacked nanosheets with a whole particle size range of 0.8–1.5 μm. The thickness of the nanosheet in VS_2-SNSs is estimated to be around 20 nm. While the VS_2-MNSs stack up randomly with microplates with whole size of more than 5 μm. The morphology and detailed crystal structure of VS_2-SNSs are further revealed by transmission electron microscopy (TEM) (Fig. 1c) and high-resolution transmission electron microscopy (HRTEM) (Fig. 1d). The HRTEM image from the edge of the nanosheet in Fig. 1c reveals that each nanosheet is an accumulation of the [001] oriented sheets with interlayer spacing around 5.76 Å. The phase of the as-prepared samples was identified by XRD (Fig. 1e). All the characteristic peaks of VS_2-SNSs and VS_2-MNSs material can be indexed into hexagonal VS_2 phase (space group: *P*-3*m*1) (JCPDF No. 01-089-1640) without impurity. The diffraction peaks of the VS_2-SNSs are more broaden and lower in intensity, which demonstrates the smaller crystalline size of the VS_2-SNSs. Raman spectra (Fig. 1f) were measured to further confirm the structure of the two samples. Both the two samples exhibit three peaks. The typical peak located at 282 cm^{-1} is associated with the E_{1g} mode of hexagonal VS_2 originated from a curvature of VS_2 sheets. Another two bands located at 389 and 406 cm^{-1} are mostly attributed to the in-plane (E^1_{2g}) displacements of vanadium and out-of-plane (A_{1g}) symmetric displacements of sulfur atoms along the *c*-axis vibration modes, respectively [46]. Moreover, the energy dispersive X-ray spectrometric (EDS) mapping (Fig. 1g) of the VS_2-SNSs confirms the existence and uniform distribution of V and S. Nitrogen sorption isotherms were measured to investigate the Brunauer-Emmet-Teller

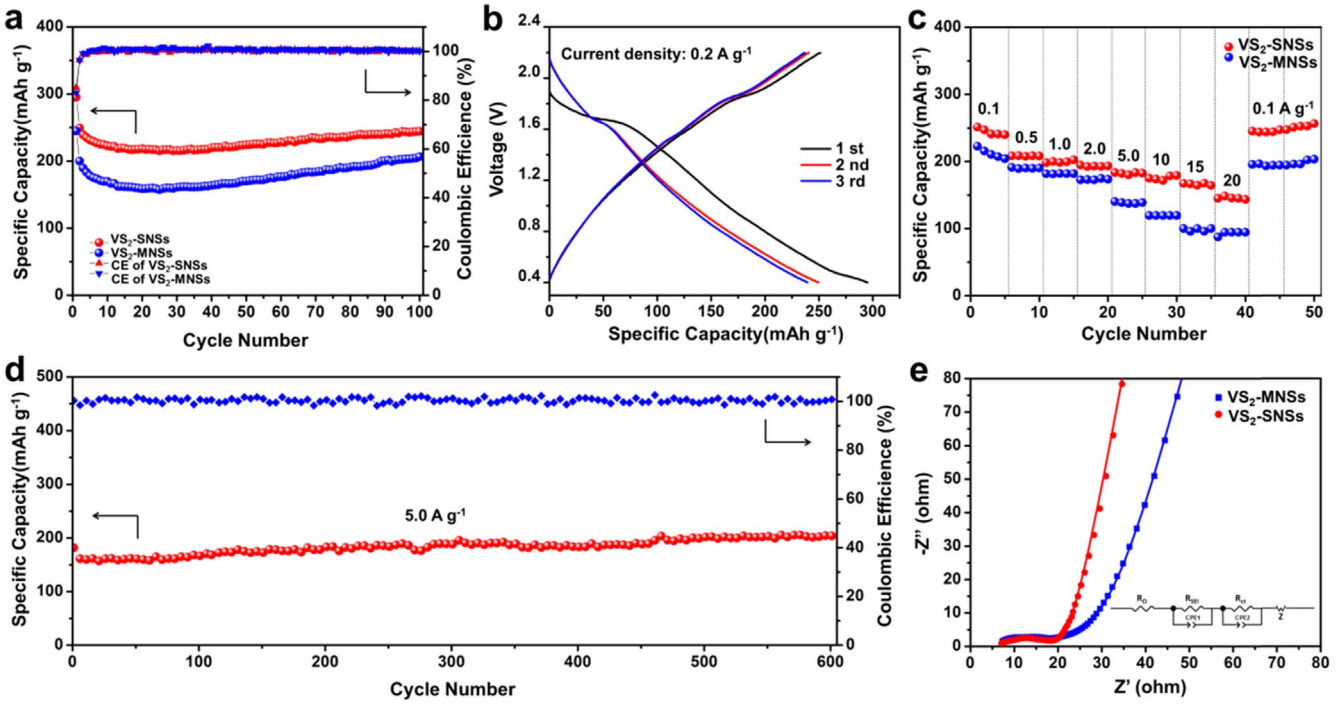

Fig. 2. (a) Cyclic performance of VS_2-SNSs and VS_2-MNSs at current density of 0.2 A g^{-1}. (b) Discharge-charge curves of the VS_2-SNSs electrode in the voltage range of 0.4–2.2 V at 0.2 A g^{-1}. (c) Rate performance of VS_2-SNSs and VS_2-MNSs. (d) Cyclic performance of VS_2-SNSs at a current density of 5.0 A g^{-1}. (e) Nyquist plots of VS_2-SNSs and VS_2-MNSs at initial state.

(BET) surface area and pore size distribution of the samples (Fig. S5). The surface area of the VS_2-SNSs is 54.1 m^2 g^{-1}, which is 2.6 times higher than that of VS_2-MNSs (20.9 m^2 g^{-1}). The nitrogen adsorption-desorption curve of VS_2-SNSs exhibits a typical hysteresis loop that can be linked to the slit-shaped pores. The pore sizes in VS_2-SNSs are mainly below 4 nm and the pore volume in VS_2-MNSs is lower than VS_2-SNSs. This result indicates that VS_2-SNSs have the larger contact area with the electrolyte, which increases the reaction sites and enhances charge transfer during cycling, resulting in the improvement of electrochemical performance.

The electrochemical performance of both VS_2-SNSs and VS_2-MNSs is shown in Fig. 2. Cycling performance of VS_2-SNSs and VS_2-MNSs at 0.2 A g^{-1} are shown in Fig. 2a. The VS_2-SNSs manifest better cycling performance than the VS_2-MNSs. The VS_2-SNSs deliver an initial discharge capacity of 295 mA h g^{-1} with a high initial coulombic efficiency (CE) of 85%. The second discharge capacity is 250 mA h g^{-1}. The capacity maintains 245 mA h g^{-1} after 100 cycles (capacity retention of 98% compared with the second cycle). The CE gradually increases to 100% after a few cycles and then can be stabilized. Fig. 2b displays the typical charge and discharge curves of the VS_2-SNSs electrode at 0.2 A g^{-1}. Rate performance at progressively increased current density (ranging from 0.1 to 20 A g^{-1}) was measured (Figs. 2c and S6). The VS_2-SNSs exhibit better rate performance than those of VS_2-MNSs. It can be seen that specific capacities of VS_2-SNSs anode are as high as 252, 203 and 180 mA h g^{-1} at 0.1, 5 and 10 A g^{-1}, respectively. When the current density is reduced from 20 A g^{-1} to 0.1 A g^{-1}, almost 100% of the initial capacity can be recovered for the VS_2-SNSs, while around 83% of the initial capacity can be recovered for the VS_2-MNSs. A capacity of 150 mA h g^{-1} can be achieved even at an extremely high-rate of 20 A g^{-1} (discharge/charge in 27 s). At a high current density of 5 A g^{-1}, the capacity of VS_2-SNSs increases gradually with cycling and reaches 204 mA h g^{-1} after 600 cycles (Fig. 2d), demonstrating superior long life performance. The discharge-charge curves of VS_2-SNSs electrode after 600 cycles are shown in Fig. S7. The increased capacity might due to the electrochemical milling effect that the active electrode material becomes smaller with the increase of cycle numbers and more active sites are exposed for sodium ion storage [47]. The increased capacity is similar to the report of MoS_2 with expanded layers [38]. In addition, the long cycling performance of VS_2-SNSs at ultra-high rate of 20 A g^{-1} is provided. After a few cycles of activation as well as an initial irreversible capacity loss, the VS_2-SNSs electrodes show almost no degradation for the next 4000 cycles (Fig. S8). Galvanostatic intermittent titration technique (GITT) studies on the VS_2 electrode indicate that the cell shows slight sloped discharge/charge profile, with a short ~1.7 V discharge plateaus for sodium storage (Fig. S9). To provide further insight, the electrochemical impedance spectra (EIS) were measured (Fig. 2e). The EIS spectra show a compressed semicircle in the high to medium frequency region of each spectrum, which corresponds to the charge transfer resistance (R_{ct}) of the electrode, and an approximately 45° inclined line in the low frequency range which stands for the Warburg impendence (Z_w). In the equivalent circuit, R_Ω represents the Ohmic resistance of the electrode system, including the electrolyte and the cell components. R_{SEI} and R_{ct} represent the resistance related to solid electrolyte interface (SEI) and the charge transfer, respectively. CPE_1, CPE_2 and Z_w are the capacitance related to SEI, the double layer and the Warburg impedance, respectively. The charge transfer resistances of the VS_2-SNSs and the VS_2-MNSs are determined to be 18 and 23 Ω, respectively. Moreover, the slope in the low frequency range of the VS_2-SNSs is larger than VS_2-MNSs. The sodium ion diffusion coefficient value (D) can be calculated using the following equation:

$$D = 0.5(RT/An^2F^2C\sigma)^2$$

where D represents the diffusion coefficient (cm^2 s^{-1}), R represents the gas constant, T represents the absolute temperature, A represents the surface area of the anode (cm^2), n is the number of electrons transferred electrochemical reaction, F is the Faraday constant, C represents the concentration of ions and σ is the Warburg factor relative to Z_{re} [48]. From the following equation, σ can be obtained (Fig. S10).

$$Z_{re} = R_D + R_L + \sigma\omega^{-1/2}$$

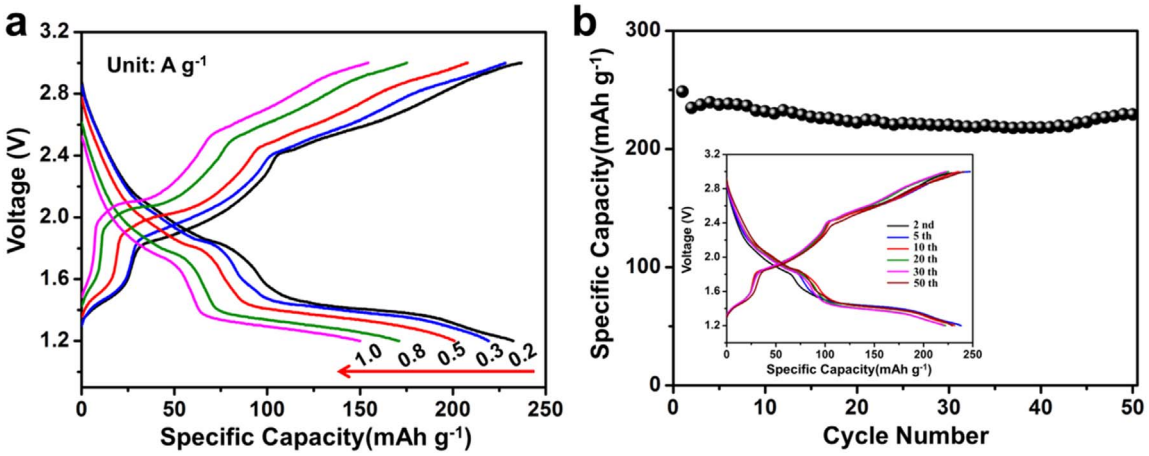

Fig. 3. (a) Discharge-charge curves of VS_2-SNSs//$Na_3V_2(PO_4)_3$/C sodium ion full cell at various rates in the voltage range of 1.2–3.0 V at 0.2 A g^{-1}. (b) Cyclic performance of the full cell at 0.2 A g^{-1} (inset is the discharge-charge curves of VS_2-SNSs//$Na_3V_2(PO_4)_3$/C sodium ion full cell at different cycles).

The ions diffusion coefficients at room temperature are calculated to be 1.54×10^{-8} and 1.52×10^{-9} cm^2 s^{-1} for the VS_2-SNSs and VS_2-MNSs, respectively, indicating the VS_2-SNSs have better Na^+ diffusion ability. The remarkable electrochemical performance of VS_2-SNSs can be attributed to their unique structure. Firstly, VS_2-SNSs with larger surface area provide more active sites, larger electrode-electrolyte contact area and enhance charge transfer than VS_2-MNSs, resulting in rapid ion diffusion and high-rate capability. Secondly, the VS_2-SNSs have a highly stable framework and can offer free space for facile strain relaxation for volume expansion during cycling, which ensures the cycling stability.

A sodium-ion full cell was also demonstrated using VS_2 as anode and $Na_3V_2(PO_4)_3$/C as cathode. Preliminary results show the full cell delivers an average operating voltage plateau at ~1.5 V and high rate and excellent cycling performance (Fig. 3).

To study the structure stability of the VS_2-SNSs during Na^+ insertion/extraction, *in-situ* XRD and *ex-situ* TEM are performed (Fig. 4). For the *in-situ* XRD, selected acquisition windows are chosen to *in situ* monitor the (100) and (011) diffractions of VS_2 during the discharge/charge processes at 0.2 A g^{-1} (Fig. 4a). When the sodium ions insert into the sample, the (100) and (011) reflections gradually shift to lower two theta angle. With the intercalation of nearly 0.16 Na^+ per formula, the (100) and (011) reflections disappear along with the appearance of two new peaks at 29.2° and 34.3°, indicating the formation of a new phase ($VS_2+xNa^++xe^-\rightarrow Na_xVS_2$, as is discussed in Eq. (S1)). These two new peaks are assigned to the (101) and (104) reflections of the $NaVS_2$ (JCPDF No. 03-065-3668), respectively. During extraction, the process is fully reversible. The (100) and (011) reflections of VS_2 are recovered until nearly 0.52 Na^+ per formula are extracted from the $NaVS_2$. At the end of charge process, all the peaks of VS_2 can be recovered. At the later cycling, the *in-situ* XRD patterns show a continuous structure change between VS_2 and $NaVS_2$. To further understand the mechanism of sodium storage, *ex-situ* HRTEM and selected area electron diffraction (SAED) measurements were employed to analyze the composition and the structure of the sodiated and desodiated VS_2 electrode. When the electrode discharged to 0.4 V, the typical HRTEM image (Fig. 4b) shows clear lattice fringes of 6.56 Å and 3.28 Å, which is in agreement with the (003) and (006) planes of $NaVS_2$, respectively. The SAED pattern (Fig. 4c) also shows that the discharge product is $NaVS_2$. When the electrode charged to 2.2 V, the structure of VS_2 recovers. The HRTEM image (Fig. 4d) shows a clear lattice spaces of 5.76 Å corresponding to the (001) plane of VS_2. All diffraction fringes in SAED pattern (Fig. 4e) can be well indexed to VS_2 phase. This result fits well with the reaction mechanism concluded from *in-situ* XRD. The crystal structures of VS_2 and $NaVS_2$ are shown in Fig. 4f. They have similar layered structures. During the electrochemical reaction, the Na ions insert into the VS_2 layers to form $NaVS_2$ without significantly change of the crystal structure. Cutting-off voltage plays an important role in achieving such good performance. High initial capacity is obtained in the voltage range of 0.01–2.2 V, but the capacity fades fast at 0.2 A g^{-1} (Fig. S11). *Ex-situ* XRD patterns (Fig. S12) confirmed the formation of Na_2S when the terminal voltage is controlled to 0.01 V, demonstrating that a conversion reaction occurs. The parent crystalline structure is completely destroyed and does not reform after the Na^+ is removed. This phenomenon is similar to other transition metal sulfides [12,35,38]. Furthermore, we recorded the TEM and HRTEM images of the origin VS_2-SNSs electrode and charged electrode after 300 and 600 cycles (Figs. S13 and S14). All HRTEM images show clear lattice fringes, indicating the high crystallinity of the sample. The results show that the whole morphology still keeps well after long cycling and the VS_2 layers are gradually expanded with the increase of cycle number, leading to more exposed active sites. The gradually expanded interlayers lower the diffusion energy barrier of Na ions and provide more active sites for sodium storage, thus the capacity increases with cycling [25]. This phenomenon doesn't emerge in VS_2 SIBs when the terminal voltage is controlled to 0.01 V. The morphology (Fig. S15) of the electrode is completely destroyed only after 1 cycle.

To further explore the nature of the charge storage process, cyclic voltammetry (CV) measurements were conducted to gain further insight into the electrochemistry of the VS_2/Na cell. The CV curves at different scan rates from 0.2 to 1 mV s^{-1} were recorded (Fig. 5a). At 0.2 mV s^{-1}, the cathodic peak at 1.65 V corresponds to the phase transformation from VS_2 to Na_xVS_2, and the anodic peaks at 1.9 V corresponds to the phase transformation from Na_xVS_2 back to VS_2. The CV curves match well with the discharge-charge curves (Fig. 4a). The curves show similar shapes during both cathodic and anodic processes at each scan rate. A small peak shift is displayed if the scan rate increases from 0.2 to 1 mV s^{-1}, demonstrating low polarization of VS_2-SNSs in the diglyme (DGM) electrolyte. A related analysis can be performed regarding the behavior of the peak current by assuming the current (i) obeys a power law relationship with the scan rate (v): $i=av^b$ (a, b are adjustable values) [12]. The b-value is determined by the slope of the ln(v)-ln(i) plots. When b-value approaches to 1, the system is mainly controlled by capacitance, while b-value is closed to 0.5, the intercalation process dominates. Fig. 5b shows the b-value at different oxidation and reduction state. As the b-value approaches 1, the battery is mainly controlled by the capacitive process. The b-value analysis for VS_2-SNSs and VS_2-MNSs was performed using the CV data between 1.6 and 2.2 V (Fig. S16). The b-value of VS_2-SNSs is higher than VS_2-

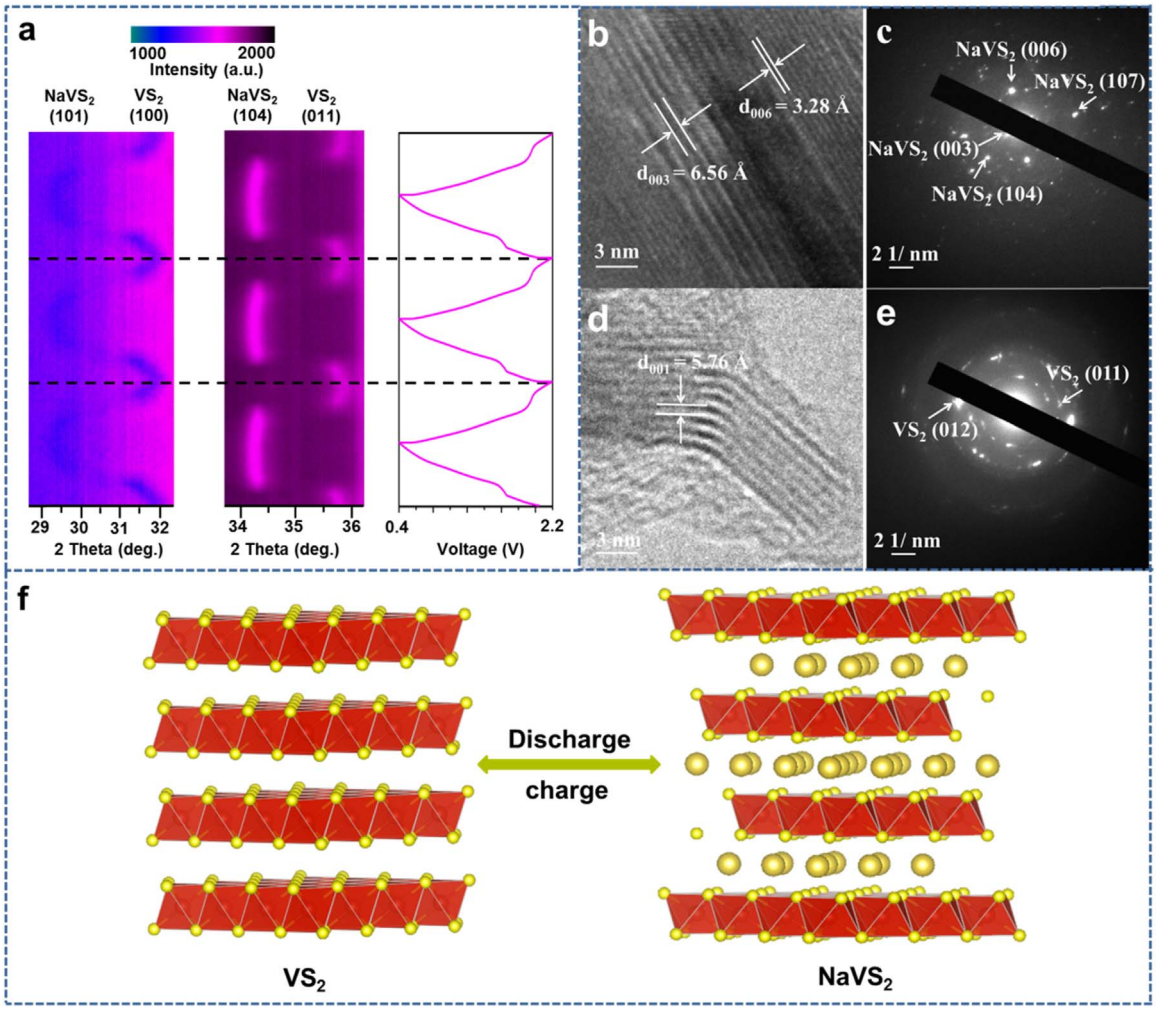

Fig. 4. (a) *In-situ* XRD patterns during galvanostatic charge and discharge at 0.2 A g^{-1}. HRTEM images and SAED patterns of VS_2-SNSs. (b, c) After discharged to 0.4 V. (d, e) After charged to 2.2 V. (f) Crystal structure transformation from VS_2 to $NaVS_2$.

MNSs at each potential, showing VS_2-SNSs have improved capacitive behavior than VS_2-MNSs. The obtained experimental results are higher than the theoretical capacity, which could be ascribed to the capacitive capacity. The capacitive capacity is contributed to the faradaic charge transfer process through surface atoms and the non faradaic double layer effect, which contribute to the extra capacity.

Another analysis is also performed to determine the regions where the capacitive contributions occur in the CV plots. We use the analysis proposed by Dunn and co-workers [35] to further quantify the capacitive and diffusion-controlled contributions to the whole capacity. The total current response (i) at a fixed potential (V) can be separated into two mechanisms of capacitive ($k_1\nu$) and diffusion-controlled processes ($k_2\nu^{1/2}$), according to the following equation:

$$i(\mathrm{V}) = k_1\nu + k_2\nu^{1/2}$$

69% and 57% of the total charge come from capacitive contribution at a scan rate of 1 mV s^{-1} for VS_2-SNSs and VS_2-MNSs (Figs. 5c and S17), respectively. This obviously implies that VS_2-SNSs offer more active surface sites than VS_2-MNSs due to the porous structure leading to fast Na^+ insertion/extraction and enhanced capacity and rate performance. Capacity contribution of VS_2-SNSs at different scan rates is showed in Fig. 5d. The capacitive contribution increases with the increase of scan rate. The kinetic analysis (Fig. 5b and c) shows that a large fraction of the stored charge comes from a capacitive process. The unique layer-by-layer stacked structure with considerable amounts of pores between the layers provides more active sites for fast Na+ diffusion, short sodium ion diffusion pathway as well as good electrolyte accessibility to all the electroactive surfaces. Thus, it's not surprising that this structure contributes the most of pseudocapacitance.

The reversible capacity and average voltage for the layered intercalation based SIBs anodes are summarized (Fig. 6). The capacity of most intercalation SIBs anodes is under 180 mA h g^{-1} and the usable capacity is located near the sodium plating voltage, leading to potential safety concerns. The VS_2 in this work stands out among those of SIBs anodes. The VS_2, which has metallic behavior, delivers a high intercalation capacity of 250 mA h g^{-1}. The specific capacity of this material is higher than most of intercalation-type SIBs anodes. These advantages make the VS_2 as one of the most promising candidates among currently studied anode materials for rechargeable energy storage (see Table S1).

4. Conclusion

Novel layer-by-layer VS_2-SNSs are synthesized using a facile one-step PVP assisted assembly method. With a highly stable framework and mesoporous structure, the electrode shows excellent electrochemical performance in SIBs. A reversible discharge capacity of 250 mA h g^{-1} is achieved at 0.2 A g^{-1}. Even at an ultrahigh current density of 20 A g^{-1}, a specific capacity of 150 mA h g^{-1} reaches (discharged/charged in 27 s). The layer-by-layer VS_2-SNSs deliver long

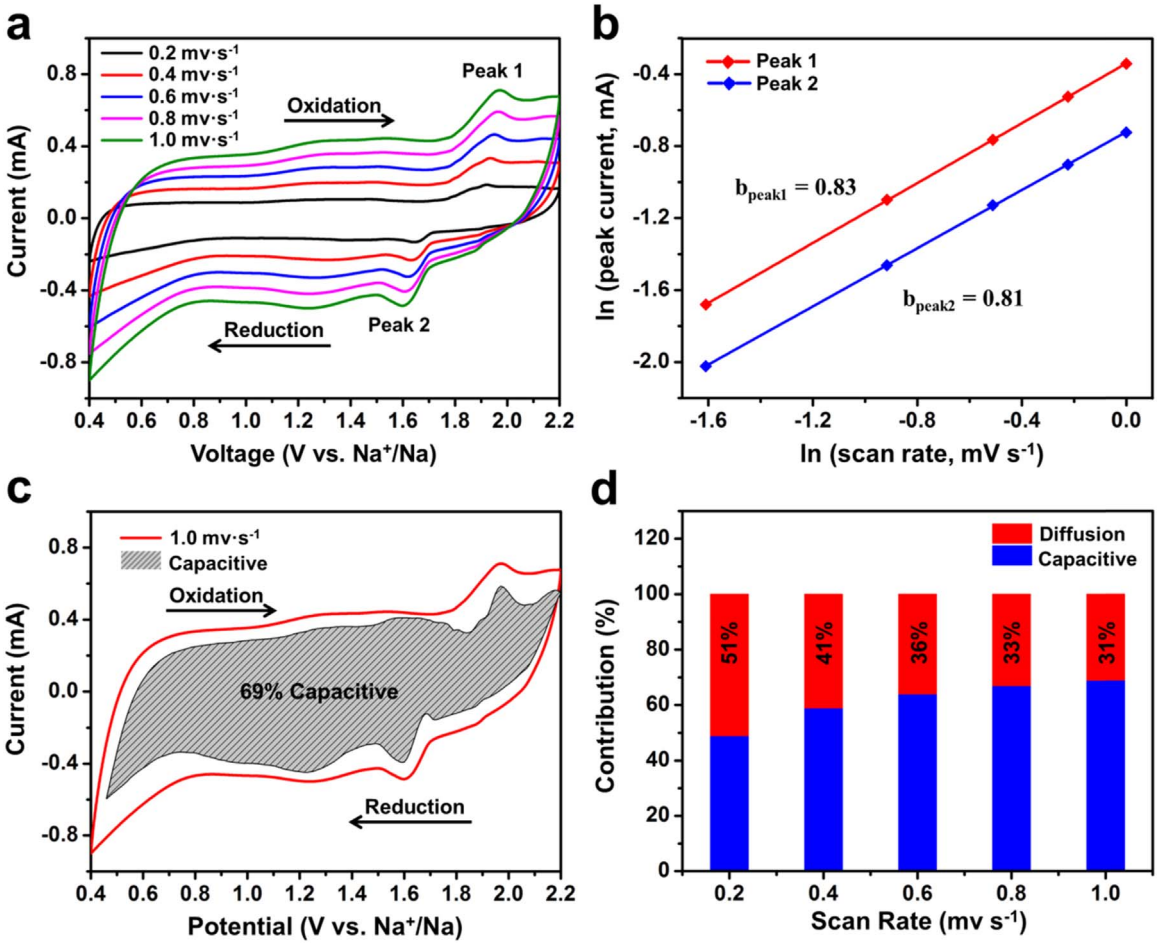

Fig. 5. (a) CV curves of the cell at different sweep rates after two cycles. (b) The fitted lines and ln (peak current) *versus* ln (scan rate) plots at different oxidation and reduction state. (c) The capacitive contribution (1 mV s^{-1}) is 69% and is shown by the shaded region. (d) The capacity contribution at different scan rates (0.2, 0.4, 0.6, 0.8 and 1.0 mV s^{-1}). The results correspond to the cells with VS_2-SNSs.

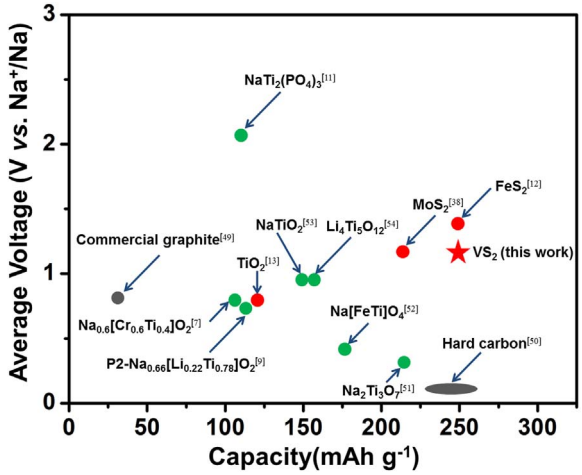

Fig. 6. Average voltage *versus* reversible capacity of intercalation based anode for various reported sodium-ion battery applications: Carbonaceous materials (grey circles) [49,50], layered sodium metal oxides and phosphates (green circles) [7,9,11,51–54] and transition metal oxide and dichalcogenides (red circles) [12,13,38].

lifetime with excellent capacity retention even after 600 cycles at 5 A g^{-1}. It's remarkable to find that a reversible intercalation reaction occurs during cycling on the base of *in-situ* XRD and *ex-situ* TEM characterization. A detailed electrochemical kinetic analysis reveals that the energy storage depends on intercalation pseudocapacitive mechanism with a high capacitive contribution up to 69% for the total capacity at 1 mV s^{-1}. The impressive electrochemical performance reveals that the VS_2 anode has great potential for next generation large scale energy storage. Besides, our findings give the opportunity for developing electrode materials of SIBs using these types of materials, which represent a commendable direction of promising rechargeable electrode materials for next generation large scale energy storage.

Acknowledgements

This work was supported by the National Key Research Program of China (2016YFA0202603), the National Basic Research Program of China (2013CB934103, 2012CB933003), the International Science & Technology Cooperation Program of China (2013DFA50840), the National Natural Science Foundation of China (51521001, 51272197, 51302203), the National Natural Science Fund for Distinguished Young Scholars (51425204), the Hubei Province Natural Science Fund for Distinguished Young Scholars (2014CFA035), the Fundamental Research Funds for the Central Universities (WUT: 2016III013, 2016IVA090, 155101003, 2016III001, 2016III002, 2016III003) and the International Postdoctoral Exchange Fellowship Program (20160025). Prof. Liqiang Mai gratefully acknowledged financial support from China Scholarship Council (No. 201606955096). Thanks to Prof. D.Y. Zhao of Fudan University and Prof. C. M. Lieber of Harvard University for strong support and stimulating discussions.

Appendix A. Supplementary material

Supplementary data associated with this article can be found in the online version at http://dx.doi.org/10.1016/j.nanoen.2017.03.036.

References

[1] M. Armand, J.M. Tarascon, Nature 451 (2008) 652–657.
[2] Y. Luo, M.S. Balogun, W. Qiu, R. Zhao, P. Liu, Y. Tong, Chem. Commun. 51 (2015) 13016–13019.
[3] X. Xia, D. Chao, Y. Zhang, J. Zhan, Y. Zhong, X. Wang, Z.X. Shen, J. Tu, H.J. Fan, Small 12 (2016) 3048–3058.
[4] Q. An, F. Lv, Q. Liu, C. Han, K. Zhao, J. Sheng, Q. Wei, M. Yan, L. Mai, Nano Lett. 14 (2014) 6250–6256.
[5] S. Wang, L. Wang, Z. Zhu, Z. Hu, Q. Zhao, J. Chen, Angew. Chem. Int. Ed. 53 (2014) 5892–5896.
[6] H.W. Lee, R.Y. Wang, M. Pasta, S.W. Lee, N. Liu, Y. Cui, Nat. Commun. 5 (2014) 5280.
[7] Y. Wang, R. Xiao, Y.S. Hu, M. Avdeev, L. Chen, Nat. Commun. 6 (2015) 6954.
[8] Y. Dong, S. Li, K. Zhao, C. Han, W. Chen, B. Wang, L. Wang, B. Xu, Q. Wei, L. Zhang, X. Xu, L. Mai, Energy Environ. Sci. 8 (2015) 1267–1275.
[9] Y. Wang, X. Yu, S. Xu, J. Bai, R. Xiao, Y.S. Hu, H. Li, X.Q. Yang, L. Chen, X. Huang, Nat. Commun. 4 (2013) 2365.
[10] S. Li, Y. Dong, L. Xu, X. Xu, L. He, L. Mai, Adv. Mater. 26 (2014) 3545–3553.
[11] C. Wu, P. Kopold, Y.L. Ding, P.A. van Aken, J. Maier, Y. Yu, ACS Nano 9 (2015) 6610–6618.
[12] Z. Hu, Z. Zhu, F. Cheng, K. Zhang, J. Wang, C. Chen, J. Chen, Energy Environ. Sci. 8 (2015) 1309–1316.
[13] C. Chen, Y. Wen, X. Hu, X. Ji, M. Yan, L. Mai, P. Hu, B. Shan, Y. Huang, Nat. Commun. 6 (2015) 6929.
[14] Y. Liu, N. Zhang, L. Jiao, J. Chen, Adv. Mater. 27 (2015) 6702–6707.
[15] J. Sun, H.W. Lee, M. Pasta, H. Yuan, G. Zheng, Y. Sun, Y. Li, Y. Cui, Nat. Nanotechnol. 10 (2015) 980–985.
[16] Y.N. Ko, S.B. Park, Y.C. Kang, Small 10 (2014) 3240–3245.
[17] D. Su, K. Kretschmer, G. Wang, Adv. Energy Mater. 6 (2016). http://dx.doi.org/10.1002/aenm.201501785.
[18] C. Wu, Y. Jiang, P. Kopold, P.A. van Aken, J. Maier, Y. Yu, Adv. Mater. (2016). http://dx.doi.org/10.1002/adma.201600964.
[19] J.H. Han, S. Lee, J. Cheon, Chem. Soc. Rev. 42 (2013) 2581–2591.
[20] G.A. Muller, J.B. Cook, H.S. Kim, S.H. Tolbert, B. Dunn, Nano Lett. 15 (2015) 1911–1917.
[21] R. Sun, Q. Wei, Q. Li, W. Luo, Q. An, J. Sheng, D. Wang, W. Chen, L. Mai, ACS Appl. Mater. Interfaces 7 (2015) 20902–20908.
[22] D. Chao, C. Zhu, P. Yang, X. Xia, J. Liu, J. Wang, X. Fan, S.V. Savilov, J. Lin, H.J. Fan, Z.X. Shen, Nat. Commun. 7 (2016) 12122.
[23] J. Wang, J. Liu, H. Yang, D. Chao, J. Yan, S.V. Savilov, J. Lin, Z.X. Shen, Nano Energy 20 (2016) 1–10.
[24] T. Zhai, X. Lu, H. Wang, G. Wang, T. Mathis, T. Liu, C. Li, Y. Tong, Y. Li, Nano Lett. 15 (2015) 3189–3194.
[25] W. Zhou, Z. Yin, Y. Du, X. Huang, Z. Zeng, Z. Fan, H. Liu, J. Wang, H. Zhang, Small 9 (2013) 140–147.
[26] W. Ho, J.C. Yu, J. Lin, J. Yu, P. Li, Langmuir 20 (2004) 5865–5869.
[27] D. Lembke, S. Bertolazzi, A. Kis, Acc. Chem. Res. 48 (2015) 100–110.
[28] D.W. Murphy, C. Cros, F.J. Di Salvo, J. Waszczak, Inorg. Chem. 16 (1977) 3027–3031.
[29] C.S. Rout, B.H. Kim, X. Xu, J. Yang, H.Y. Jeong, D. Odkhuu, N. Park, J. Cho, H.S. Shin, J. Am. Chem. Soc. 135 (2013) 8720–8725.
[30] Y. Jing, Z. Zhou, C.R. Cabrera, Z. Chen, J. Phys. Chem. C 117 (2013) 25409–25413.
[31] J. Feng, X. Sun, C. Wu, L. Peng, C. Lin, S. Hu, J. Yang, Y. Xie, J. Am. Chem. Soc. 133 (2011) 17832–17838.
[32] B. Conway, V. Birss, J. Wojtowicz, J. Power Sources 66 (1997) 1–14.
[33] V. Augustyn, J. Come, M.A. Lowe, J.W. Kim, P.L. Taberna, S.H. Tolbert, H.D. Abruna, P. Simon, B. Dunn, Nat. Mater. 12 (2013) 518–522.
[34] V. Augustyn, P. Simon, B. Dunn, Energy Environ. Sci. 7 (2014) 1597–1614.
[35] J.B. Cook, H.S. Kim, Y. Yan, J.S. Ko, S. Robbennolt, B. Dunn, S.H. Tolbert, Adv. Energy Mater. 6 (2016) 1501937.
[36] C. Zhu, X. Mu, P.A. van Aken, Y. Yu, J. Maier, Angew. Chem. Int. Ed. 53 (2014) 2152–2156.
[37] L. David, R. Bhandavat, G. Singh, ACS Nano 8 (2014) 1759–1770.
[38] Z. Hu, L. Wang, K. Zhang, J. Wang, F. Cheng, Z. Tao, J. Chen, Angew. Chem. Int. Ed. 126 (2014) 13008–13012.
[39] K.M. Abraham, L. Pitts, R. Schiff, J. Electrochem. Soc. 127 (1980) 2545–2550.
[40] Z. Fang, S. Hao, L. Long, H. Fang, T. Qiang, Y. Song, CrystEngComm 16 (2014) 2404–2410.
[41] K.M. Koczkur, S. Mourdikoudis, L. Polavarapu, S.E. Skrabalak, Dalton Trans. 44 (2015) 17883–17905.
[42] J.S. Chen, J. Liu, S.Z. Qiao, R. Xu, X.W. Lou, Chem. Commun. 47 (2011) 10443–10445.
[43] Y. Li, Y. Liang, F.C.R. Hernandez, H.D. Yoo, Q. An, Y. Yao, Nano Energy 15 (2015) 453–461.
[44] Z. Ling, C.E. Ren, M. Zhao, J. Yang, J.M. Giammarco, J. Qiu, M.W. Barsoum, Y. Gogotsi, Proc. Natl. Acad. Sci. USA 111 (2014) 16676–16681.
[45] G.S. Bang, K.W. Nam, J.Y. Kim, J. Shin, J.W. Choi, S.Y. Choi, ACS Appl. Mater. Interfaces 6 (2014) 7084–7089.
[46] W. Fang, H. Zhao, Y. Xie, J. Fang, J. Xu, Z. Chen, ACS Appl. Mater. Interfaces 7 (2015) 13044–13052.
[47] K. Zhao, F. Liu, C. Niu, W. Xu, Y. Dong, L. Zhang, S. Xie, M. Yan, Q. Wei, D. Zhao, L. Mai, Adv. Sci. 2 (2015) 1500154.
[48] P. Hu, M. Yan, X. Wang, C. Han, L. He, X. Wei, C. Niu, K. Zhao, X. Tian, Q. Wei, Z. Li, L. Mai, Nano Lett. 16 (2016) 1523–1529.
[49] D. Stevens, J. Dahn, J. Electrochem. Soc. 148 (2001) A803–A811.
[50] S. Komaba, W. Murata, T. Ishikawa, N. Yabuuchi, T. Ozeki, T. Nakayama, A. Ogata, K. Gotoh, K. Fujiwara, Adv. Funct. Mater. 21 (2011) 3859–3867.
[51] J. Ni, S. Fu, C. Wu, Y. Zhao, J. Maier, Y. Yu, L. Li, Adv. Energy Mater. 6 (2016) 1502568.
[52] J. Wang, B. Qiu, X. He, T. Risthaus, H. Liu, M.C. Stan, S. Schulze, Y. Xia, Z. Liu, M. Winter, Chem. Mater. 27 (2015) 4374–4379.
[53] D. Wu, X. Li, B. Xu, N. Twu, L. Liu, G. Ceder, Energy Environ. Sci. 8 (2015) 195–202.
[54] Y. Sun, L. Zhao, H. Pan, X. Lu, L. Gu, Y.S. Hu, H. Li, M. Armand, Y. Ikuhara, L. Chen, Nat. Commun. 4 (2013) 1870.
[55] W. Ren, Z. Zheng, C. Xu, C. Niu, Q. Wei, Q. An, K. Zhao, M. Yan, M. Qin, L. Mai, Nano Energy 25 (2016) 145–153.

Ruimin Sun received her Bachelor's degree in Department of Materials Science and Engineering from Wuhan University of Technology (WUT) in 2013. She is currently working toward the Ph.D. degree and her current research focuses on the energy storage materials and devices.

Qiulong Wei received his B.S. degree in Department of Materials Science and Engineering from Wuhan University of Technology (WUT) in 2011. He received his Ph.D. degree from WUT in 2016. His current research involves the design and synthesis of novel nanomaterials for achieving both high energy density and power density electrochemical energy storage device, including the lithium-ion battery, sodium-ion battery and the hybrid capacitor.

Jinzhi Sheng received his M.S. degree in Materials Engineering from Wuhan University of Technology in 2015. He is currently working toward the Ph.D. degree and his current research focuses on the energy storage materials and devices.

Changwei Shi received his Bachelor's degree in Materials Science and Engineering from Wuhan University of Technology in 2014. He is currently working toward the Ph.D. degree and his current research focuses on the energy storage materials and devices.

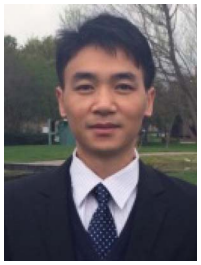

Qinyou An is Associate Professor of Materials Science and Engineering at Wuhan University of Technology (WUT). He received his Ph.D. degree from WUT in 2014. He carried out his postdoctoral research in the laboratory of Prof. Yan Yao at the University of Houston in 2014–2015. Currently, his research interest include energy storage materials and devices.

Sijie Liu is an undergraduate student and in the Department of International School of Materials Science and Engineering from Wuhan University of Technology since 2014. His current research focuses on nanoenergy materials and devices.

Liqiang Mai is Cheung Kong Scholar Chair Professor at Wuhan University of Technology (WUT), Distinguished Young Scholar for National Natural Science Fund of China, and Winner of National Ten Thousand Talent Plan of China. He received his Ph.D. degree from WUT in 2004 and carried out postdoctoral research in Prof. Zhonglin Wang's group at Georgia Institute of Technology (2006–2007). He worked as an advanced research scholar in Prof. Charles M. Lieber's group at Harvard University (2008–2011) and Prof. Peidong Yang's group at University of California, Berkeley (2017). His current research interests focus on nanowire materials and devices for energy storage.